

SUPPLEMENTAL MATERIAL

Optical evidence for a Weyl semimetal state in pyrochlore

$\text{Eu}_2\text{Ir}_2\text{O}_7$

A. B. Sushkov,¹ J. B. Hofmann,² G. S. Jenkins,¹ J. Ishikawa,³ S. Nakatsuji,³ S. Das Sarma,² and H. D. Drew¹

¹*Center for Nanophysics and Advanced Materials,
Department of Physics, University of Maryland,
College Park, Maryland 20742, USA*

²*Condensed Matter Theory Center and Joint Quantum Institute,
Department of Physics, University of Maryland,
College Park, Maryland 20742, USA*

³*Institute for Solid State Physics, University of Tokyo, Kashiwa, Chiba 277-8581, Japan*

(Dated: March 5, 2022)

I. MODEL OF SUM OF LORENTZIANS

We begin our analysis with fitting the optical data with a model dielectric function of a sum of Lorentzians. By fitting experimental reflection and transmission spectra with this model, we can get separately temperature dependence of the spectral weight and scattering rate of the free carriers (Drude term), as well as resonance frequencies, spectral weight, and scattering rate for phonons and electronic transitions. For the present system, we use a Drude term, seven expected phonons, and five electronic transitions. Five Lorentzian oscillators were found sufficient to give a very good representation of the electronic response. Figure S1(a) shows the measured reflectivity and transmission spectra of $\text{Eu}_2\text{Ir}_2\text{O}_7$ in the frequency range of phonons together with the model curves. These are the same spectra as in figure 1 of the paper but with linear frequency scale.

Figure S1(b) shows each Lorentzian term separately except for the phonons which are shown as one spectrum. The sum of these terms gives the net optical conductivity. It is clear that these components of the optical conductivity have different resonance frequencies and, especially, widths and that they do not interfere with each other in the fitting procedure. We note that the Drude term at 7 K (blue curve) is broad and it gives a small but finite dc conductivity. The fact that the Drude term (red curve) and the lowest electronic peak (magenta curve) have opposite slope allows the clean separation of their contributions by fitting the transmission spectra. We first fit simultaneously the 7 K transmission and reflection spectra. At this temperature, the transmission is maximum at low frequencies and it is a clear signature of semimetallic optical conductivity. We found that allowing for a temperature dependence of the Drude and phonon parameters is sufficient to account for the observed temperature dependence. These fit results are shown in Fig. 3 of the paper as open circles. We then fit the reflectivity spectra only at temperatures at 70 K and higher where there is no transmission for the thinned crystal at these temperatures. Again, a variation of only the Drude and phonon parameters keeping all other parameters fixed is sufficient. Results of this fit are shown in Fig. 3 as solid squares.

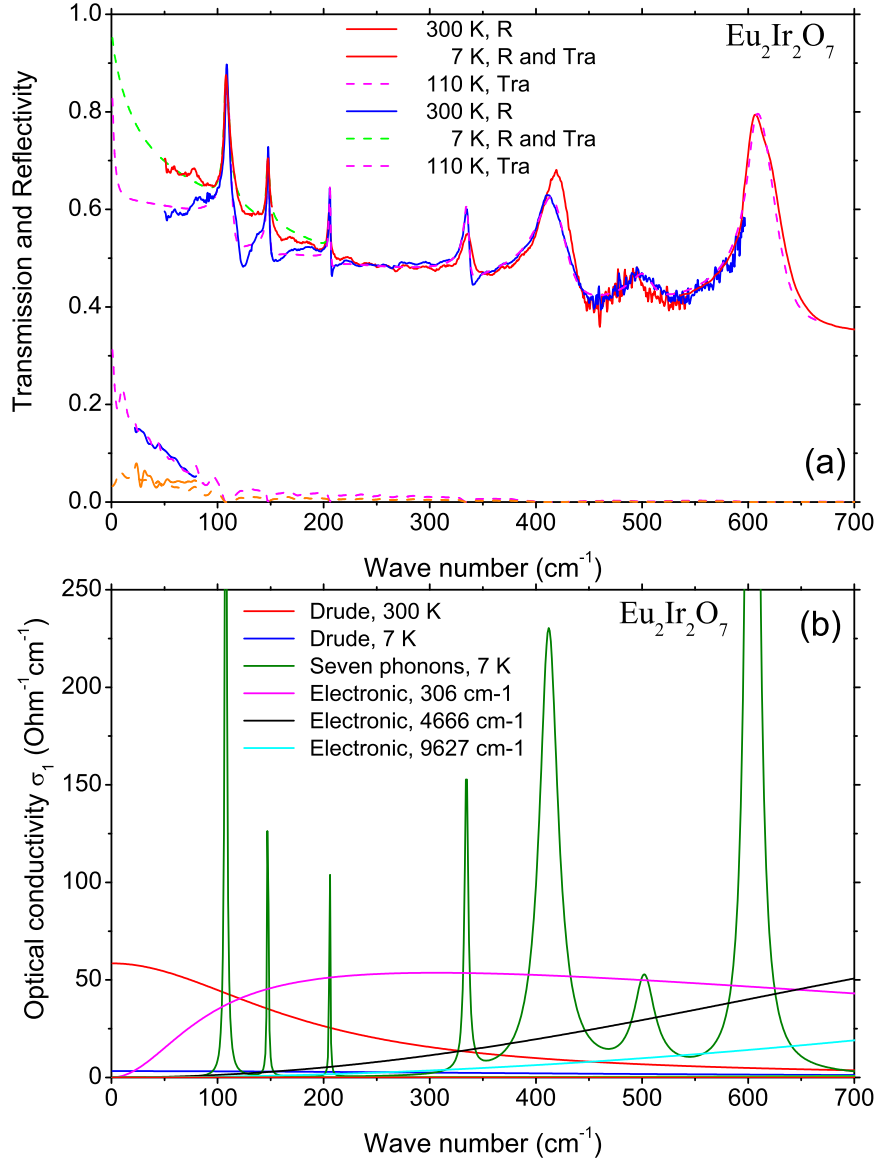


FIG. 1. (color online). (a) Reflectivity (R) and transmission (Tra) of a $\text{Eu}_2\text{Ir}_2\text{O}_7$ single crystal. Dashed curves are fits using the Lorentzian model (Eq. (1) of the paper). (b) Components of the total optical conductivity: Drude, phonons, and three lowest in frequency electronic transitions.

II. MODEL OF THE VARIATIONAL DIELECTRIC FUNCTION (VDF)

In the second method, we use the results of the first method as a starting spectrum and calculate the VDF $\varepsilon(\omega)$ [27]. This accounts for small deviations between Lorentzian fit and experimental data. Figure S2 shows an example of the two types of fit. It is apparent from the figure that the model curve (blue) for VDF fit is practically indistinguishable from

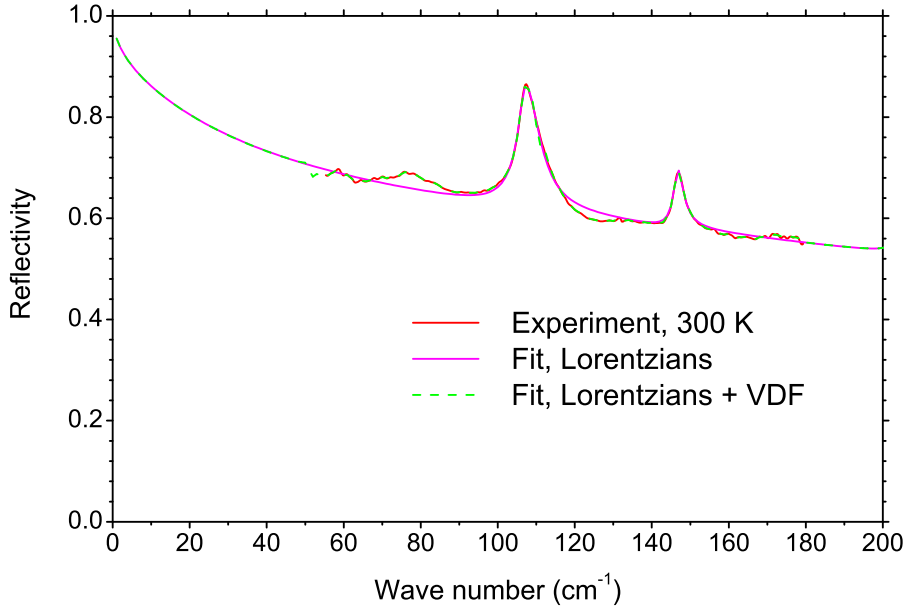


FIG. 2. (color online). Experimental and model reflectivity of a $\text{Eu}_2\text{Ir}_2\text{O}_7$ single crystal calculated from the full variational dielectric function.

the experimental curve (red). The VDF fit is equivalent to the standard Kramers-Kronig transformation technique [27] and both rely on assumed extrapolation beyond the measured interval. The value of the VDF fit is that it reproduces all small features of the spectrum not included in the sum of Lorentzians.

III. SPECTRAL WEIGHT

To check our conclusion that all temperature changes come only from the Drude and phonon terms, we use another standard spectroscopic tool — the analysis of the total spectral weight $SW(\omega)$:

$$SW(\omega_c) = \int_0^{\omega_c} \sigma_1(\omega) d\omega = \frac{\pi}{120} \omega_{pt}^2, \quad (1)$$

where σ_1 is the optical conductivity in units of $(\text{Ohm}\cdot\text{cm})^{-1}$ and the effective (or total) plasma frequency ω_{pt} includes all possible excitations. In Figure S3, we compare ω_{pt}^2 obtained by integration of the VDF optical conductivity up to the cutoff frequency $\omega_c=530 \text{ cm}^{-1}$ with the Drude weight, ω_{sD}^2 where the ω_{sD} data are the same as in Fig. 3(a) of the paper obtained from the sum of Lorentzians fit. Here, we have shifted the ω_{pt}^2 curve (blue stars) by an arbitrary constant to exclude all temperature independent excitations. We find that

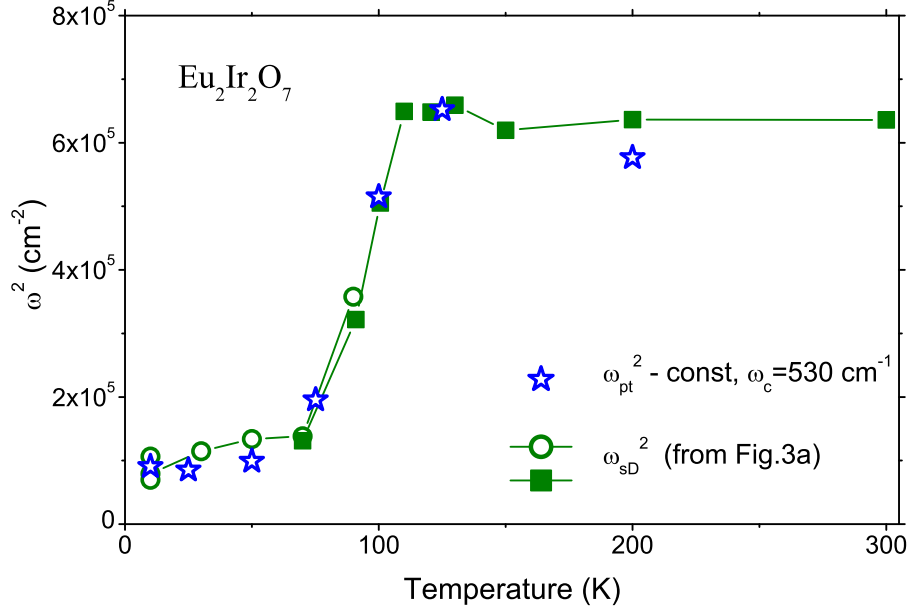


FIG. 3. (color online). Comparison of the temperature dependences of the total (stars) and Drude (open circles and solid squares) spectral weights. The total spectral weight was shifted down to exclude the temperature independent parts.

the agreement of all data is quite impressive considering that not only are they calculated differently but also they are based on different measured spectra: blue stars were obtained from the reflectivity measured with the 4 K bolometer in the frequency range 90–600 cm^{-1} , open circles and solid squares come from the transmission and reflection measured with the 1.6 K bolometer in the frequency range 10–200 cm^{-1} . From a comparison of the $\omega_{\text{pt}}^2(T)$ (total spectral weight) and the $\omega_{\text{sD}}^2(T)$ (Drude term), we conclude that only the Drude spectral weight depends on temperature. While the phonons do have temperature dependent widths their total spectral weight is practically independent of temperature compared to the Drude weight.

Optical evidence for a Weyl semimetal state in pyrochlore $\text{Eu}_2\text{Ir}_2\text{O}_7$

A. B. Sushkov,¹ J. B. Hofmann,² G. S. Jenkins,¹ J. Ishikawa,³ S. Nakatsuji,^{3,4} S. Das Sarma,² and H. D. Drew¹

¹*Center for Nanophysics and Advanced Materials, Department of Physics,
University of Maryland, College Park, Maryland 20742, USA*

²*Condensed Matter Theory Center and Joint Quantum Institute,
Department of Physics, University of Maryland, College Park, Maryland 20742, USA*

³*Institute for Solid State Physics, University of Tokyo, Kashiwa, Chiba 277-8581, Japan*

⁴*PRESTO, Japan Science and Technology Agency (JST),
4-1-8 Honcho Kawaguchi, Saitama 332-0012, Japan*

(Dated: March 5, 2022)

A Weyl semimetallic state with pairs of nondegenerate Dirac cones in three dimensions was recently predicted to occur in the antiferromagnetic state of the pyrochlore iridates. Here, we show that the THz optical conductivity and temperature dependence of the free carrier response in pyrochlore $\text{Eu}_2\text{Ir}_2\text{O}_7$ match the predictions for a Weyl semimetal and suggest novel Dirac liquid behavior. The interband optical conductivity vanishes continuously at low frequencies signifying a semimetal. The metal-semimetal transition at $T_N = 110$ K is manifested in the Drude spectral weight, which is independent of temperature in the metallic phase, and which decreases smoothly in the ordered phase. The temperature dependence of the free carrier weight below T_N is in good agreement with theoretical predictions for a Dirac material. The data yield a Fermi velocity $v_F \approx 4 \cdot 10^7$ cm/s, a logarithmic renormalization scale $\Lambda_L \approx 600$ K, and require a Fermi temperature of $T_F \approx 100$ K associated with residual unintentional doping to account for the low temperature optical response and dc resistivity.

PACS numbers: 75.47.Lx, 76.30.Kg, 78.30.-j, 71.30.+h

Condensed matter physics is in an exciting new era dominated by Dirac materials and topological effects. The introduction of topology, particularly in association with spin-orbit coupling, has led to predictions of novel electronic and optical phenomena¹⁻⁴. The most recent development is the discovery of three-dimensional (3D) Dirac⁵⁻¹⁰ and Weyl¹¹⁻¹³ materials, where the Dirac cones come in pairs and have non-Kramers degenerate chiral bands protected by topology. A 3D Weyl state has been predicted¹⁴ for the $5d$ transition metal oxide family of pyrochlore iridates¹⁵, which are strongly interacting materials with a strong spin-orbit interaction. However, in the absence of direct experimental evidence their ground state is still under intense discussion¹⁶⁻¹⁹.

The pyrochlore iridates, $R_2\text{Ir}_2\text{O}_7$, are strongly interacting materials that exhibit frustrated magnetism and an associated metal-insulator transition as R varies across the rare earth series²⁰. Due to a strong spin-orbit interaction these materials have been recognized as having potentially exotic ground states including the Weyl semimetallic state in the low temperature magnetic phase. Also, axion insulator^{14,16}, topological band insulator and Mott insulator¹, and spin liquid states^{21,22} have been proposed. X-ray diffraction experiments show that there is no structural transition breaking the cubic symmetry in Nd, Eu, and Pr pyrochlores, and that Eu compound displays a smooth thermal contraction of the lattice parameters through the "metal-insulator" transition²³. Ueda et al.²⁴ reported a 50 meV optical gap in the ground state of polycrystalline $\text{Nd}_2\text{Ir}_2\text{O}_7$ which was tuned to zero by the partial substitution of Ir by Rh and that gapless state was proposed to be a Weyl semimetal. By contrast, infrared studies of $\text{Bi}_2\text{Ir}_2\text{O}_7$ found a strongly

metallic ground state²⁵. Therefore, at present there is no clear evidence of the predicted Weyl semimetal state in the rare earth pyrochlores.

Here, we present evidence of a Weyl semimetal on the basis of experimental and theoretical studies of the optical response, and we identify the electronic phase transition in $\text{Eu}_2\text{Ir}_2\text{O}_7$ at T_N as a metal-semimetal transition in which the conductance is controlled by the thermal population of the Weyl cones. Single crystals of $\text{Eu}_2\text{Ir}_2\text{O}_7$ were grown as described elsewhere²⁶. Our crystal has the same dc conductivity as the sample #2 of Ref.²⁶. Fourier transform infrared reflectivity and transmission measurements were performed on the 1.8 mm in diameter (111) face of a single crystal. For transmission measurements at frequencies below 100 cm^{-1} , the crystal was glued down to an intrinsic Si substrate using transparent Stycast epoxy and was polished down to ≈ 10 micron.

Figure 1 shows the measured reflectivity and transmission spectra of $\text{Eu}_2\text{Ir}_2\text{O}_7$ over a broad frequency range. The transmission measured at 7 K immediately suggests a semimetallic state. The negative slope implies an optical conductivity growing with frequency. An insulator (or gapped state) would give a flat transmission, and a free carrier Drude term would give a slope of opposite sign.

We have analyzed the reflectivity and transmission spectra in two standard ways²⁷: first, using a model of a sum of Lorentzian oscillators and second, using a variational dielectric function (equivalent to a Kramers-Kronig transformation)²⁸. In the first method, we fit the reflectivity and the transmission spectra of $\text{Eu}_2\text{Ir}_2\text{O}_7$ using a Lorentzian model, in which the complex dielectric

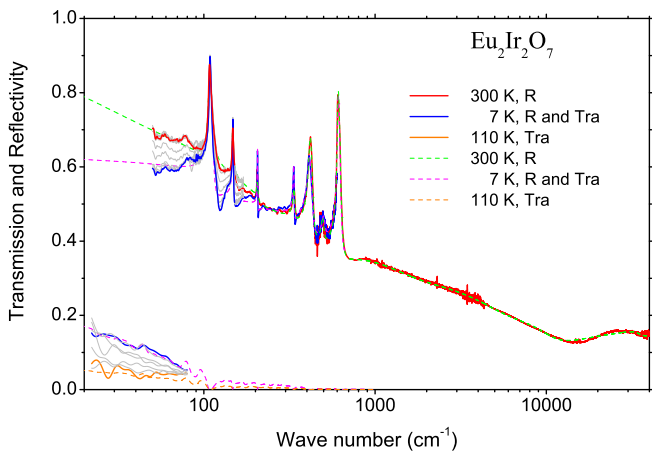


FIG. 1. (color online). Reflectivity (R) and transmission (Tra) of a $\text{Eu}_2\text{Ir}_2\text{O}_7$ single crystal. Dashed curves are fits using the Lorentzian model (Eq. (1)). Grey lines are spectra at intermediate temperatures. The temperature dependence was measured over a 20–6,000 cm^{-1} frequency range.

function $\varepsilon = \varepsilon_1 + i\varepsilon_2$ takes the form:

$$\varepsilon(\omega) = \varepsilon_\infty + \sum_j \frac{\omega_{sj}^2}{\omega_{0j}^2 - \omega^2 - i\omega\gamma_j}. \quad (1)$$

Here ω_{0j} , γ_j , and ω_{sj} are the resonance, the damping, and the spectral weight frequencies of the j th electric dipole active mode, respectively. For the present system, we use a Drude term, seven symmetry allowed phonons²⁹, and we find that the electronic response can be well represented using five electronic transitions, the lowest one at $\omega_0=306 \text{ cm}^{-1}$ with $\gamma=1143 \text{ cm}^{-1}$. In the second method, we use the results of the first method as a starting spectrum for the variational $\varepsilon(\omega)$ to account for small deviations²⁷. The complex optical conductivity is related to the dielectric function by $\sigma = \sigma_1 + i\sigma_2 = \omega\varepsilon/4\pi i$.

Figure 2 presents the frequency-dependent optical conductivity σ_1 and the dielectric constant ε_1 as obtained from the analysis of the experimental spectra. Figure 2(a) shows the optical conductivity in a broad frequency range as obtained from the variational ε analysis. The two-peak conductivity spectra are consistent with resonant inelastic X-ray scattering spectra³⁰ and band structure calculations¹⁶. The vanishing of σ_1 at low frequencies is a signature of a Dirac semimetal. The 1 eV band consists of transitions within the $J_{eff}=1/2$ bands¹⁶. Figures 2(b) and 2(c) show the optical conductivity and the dielectric constant at low frequencies. The increasing ε_1 at low frequencies (Fig. 2(c)) is another characteristic of a semimetal and is expected to diverge logarithmically for an intrinsic Weyl semimetal in the absence of disorder³¹. The optical conductivity of an intrinsic Weyl semimetal can be written as

$$\sigma_1 = \frac{g}{12} \cdot \frac{e^2}{h} \cdot \frac{\omega}{\bar{v}_F} \quad (2)$$

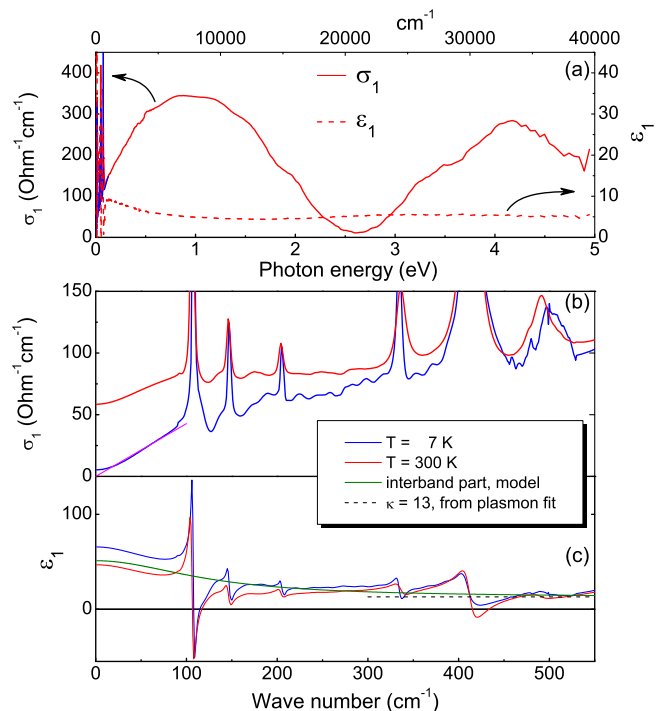


FIG. 2. (color online). Optical conductivity and dielectric constant of a $\text{Eu}_2\text{Ir}_2\text{O}_7$ single crystal. (a) Temperature-independent broad band electronic optical conductivity. (b) Temperature-dependent low-frequency part of the optical conductivity. Our zero frequency values are close to the dc measurements²⁶. The magenta line is a linear fit of equation (2) to the conductivity. (c) The dielectric constant. The continuous green line is the blue 7 K line with the phonon contributions removed. The dashed black line denotes the high-frequency dielectric constant κ obtained from the plasmon fit.

arising from interband excitations within the Dirac cone¹⁴. Here, we denote by g the degeneracy of Dirac nodes and by $\bar{v}_F = (v_F^x v_F^y v_F^z)^{1/3}$ the geometric mean of the Fermi velocities. By fitting this expression to the optical conductivity (magenta line in Fig. 2(b)) using $g=24$ ¹⁴, we obtain $\bar{v}_F = 3.4 \cdot 10^7 \text{ cm/s}$.

Based on this fit to the optical conductivity, we can extract the Coulomb interaction strength in the semimetal as given by the effective Dirac fine structure constant $\alpha = e^2/\hbar v_F \kappa$. Here, κ which is of the order of 10 is the high-frequency dielectric constant which shows no temperature-dependence as is evident in Fig. 2(c). (We use ε and κ to designate experimental and theoretical dielectric constant, respectively.) This gives a bare value of $\alpha=0.7$ for the interaction strength, indicating that electron interaction could have considerable impact on the low-energy properties of this Dirac material. Since the corresponding fine structure constant for quantum electrodynamics is 1/137, the current problem is a strong-coupling (and non-relativistic) version of quantum electrodynamics.

The conductivity exhibits a temperature dependence

only at low frequencies $\omega < 500 \text{ cm}^{-1}$. Fits of the Eq. (1) to the experimental spectra reveal that only the Drude and phonon terms are temperature dependent while the interband conductivity can be kept constant at all temperatures. The validity of this conclusion is verified by a spectral weight analysis presented in the Supplemental Material²⁷. We show the result for the experimental Drude spectral weight and scattering γ as a function of temperature in Fig. 3(a,b). The metal-semimetal transition at T_N is manifested as a smooth decrease of the Drude spectral weight in the Weyl state which can exist only below T_N where time-reversal symmetry is broken¹⁴.

In Fig. 3(a), we compare the experimental Drude weight with the theoretical prediction for a Dirac liquid. The low-temperature saturation indicates a finite Fermi energy E_F (associated with unintentional residual doping), leads to a low temperature dc conductivity and marks a transition between an extrinsic metallic low-temperature regime ($k_B T < E_F$) and an intrinsic semimetallic high-temperature regime ($k_B T > E_F$). Our observations are consistent with the Drude weight as predicted by kinetic theory

$$\omega_{sD}^2 = -\frac{e^2 \bar{v}_F^2}{3} \int_{-\infty}^{\infty} dE D(E) \frac{\partial f(E)}{\partial E}, \quad (3)$$

where $D(E) = gE^2/[2\pi^2(\hbar\bar{v}_F)^3]$ is the density of states and $f(\varepsilon)$ the Fermi-Dirac distribution. A fit of the Drude weight (solid black line in Fig. 3(a)) gives a finite Fermi energy of $E_F/k_B \approx 70 \text{ K}$ and a Fermi velocity of $\bar{v}_F = 4 \cdot 10^7 \text{ cm/s}$, in agreement with the direct fit to the frequency-dependent conductivity. For comparison, we include a fit to the high-temperature Drude weight in the strictly intrinsic limit (dashed blue line in Fig. 3(a)) which shows that finite doping does not affect the Drude weight at high temperature ($k_B T > E_F$). Note that for a general semimetallic dispersion $E \sim |k|^z$, the Drude weight is expected to scale as $\omega_{sD}^2 \sim T^{1+1/z}$ with temperature³². The superlinear temperature dependence implies $z < 1$ in this effective model, compellingly excluding, for example, a parabolic semimetallic ground state.

Our experimental Drude weight is seen to deviate from the strict linear temperature scaling of a noninteracting semimetal, which can be attributed to electron interactions: the interaction strength of an intrinsic Dirac semimetals acquires a scale-dependence due to ultraviolet renormalization, giving rise to a superlinear temperature dependence of the Drude weight and providing a direct signature of electron interaction effects^{31,33}. Within RPA, the temperature dependence of the interaction strength is given by^{33,34}

$$\alpha(T) = \frac{3\pi}{g} \ln^{-1} \frac{\Lambda_L}{T}. \quad (4)$$

Instead of depending on e^2 , \bar{v}_F , and κ separately, this expression contains a single renormalized energy scale Λ_L , the Landau pole, at which the coupling α diverges. This

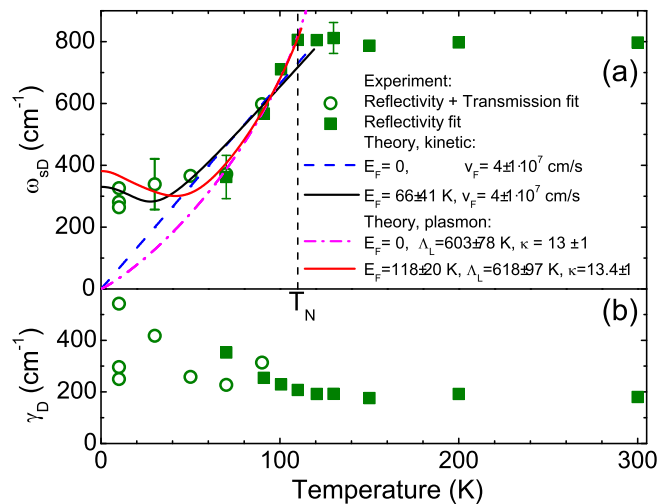


FIG. 3. (color online). Temperature dependence of the spectral Drude weight and scattering rate γ . (a) Open circles — results of simultaneous fit of reflectivity and transmission, solid squares — results of reflectivity fits, both using Eq. (1), lines — fits of kinetic theory (Eq. (3)) and plasmon to these experimental points below T_N . (b) Experimental scattering rate of free carriers.

Landau scale is an effective parameter of the system that can be extracted from measurements of the Drude weight and corresponds to a cutoff scale beyond which the Dirac dispersion is no longer linear. In the present system, it can be associated with the Lifshitz saddle point between each pair of Weyl points³³.

In the absence of disorder and phonon contributions, the Drude weight corresponds to the plasmon frequency as defined by the zero of the dielectric function $\varepsilon(\omega) = \kappa_0 - \omega_{sD}^2/\omega^2$. We assume κ_0 independent of T and ω (Fig. 2(c)) and it is a good assumption in the frequency range $300\text{--}800 \text{ cm}^{-1}$ where solutions for ω_{sD} are found. We perform a fit to the experimental ω_{sD} using the plasmon dispersion of an extrinsic Dirac semimetal³³, which fully takes into account the competing effects of finite doping and renormalization of the interaction. Since theoretical calculations only predict the renormalization of the effective fine structure constant α , there is a question whether renormalization effects should be manifested in the Drude weight, the dielectric constant, or both. The result of the fit is shown in Fig. 3(a) as a red solid line. We obtain good agreement with the experiment with an effective static dielectric constant of $\kappa_0 \approx 13$ and a Fermi energy of $E_F/k_B \approx 100 \text{ K}$, which is consistent with the experimental dielectric function ε_1 (Fig. 2), and the fit to the Drude-Boltzmann weight (Eq. 3), respectively. The Landau pole takes an anomalously small value of $\Lambda_L \approx 600 \text{ K}$, giving rise to strong superlinear scaling. This could be taken as an indirect sign that the material hosts pairs of Weyl cones in close proximity, consistent with the picture of a Weyl semimetal state with broken time-reversal symmetry. For comparison, we also include a fit of the intrinsic finite-temperature plasmon in Fig. 3(a)

(dash-dotted magenta line). As before, the intrinsic re-
sult captures the high-temperature behavior where the
Weyl state is most expected and the saturation at low
temperature can be attributed to finite doping. Intu-
itively, one could expect a characteristic step in $\sigma_1(\omega)$ at
 $2E_F \approx 140 \text{ cm}^{-1}$ but it should be smeared out by large
scattering rate and cannot be seen clearly in Fig. 2(b).

Linear (or quasi-linear) dependence of the low fre-
quency optical conductivity — a signature of a Dirac
semimetallic state — has also been recently reported in
several other 3D materials: HgCdTe³⁵, quasicrystals³⁶,
and ZrTe₅³⁷. A notable result of our work compared
to previous studies is the excellent agreement of the ex-
perimental and theoretical temperature dependent Drude
spectral weight providing strong evidence of a Weyl state
with finite doping. However, the independence of the
Drude parameters on temperature in the paramagnetic
state above T_N is surprising and merits further study.

In summary, the optical response of a Eu₂Ir₂O₇ single
crystal reveals a semimetallic electronic structure with
approximately linear frequency dependence of the opti-
cal conductivity down to 3 meV at low temperature.
Below T_N , the Drude spectral weight diminishes con-
sistent with the reduced thermal excitations of a Weyl
semimetal. This means that the long-thought “metal-
insulator” transition in pyrochlore iridates may actually

be a metal-semimetal transition, at least, in the case of
Eu₂Ir₂O₇. These two data sets can be modeled assum-
ing a Weyl state, as 24 Weyl cones with an average Fermi
velocity $\bar{v}_F = 4 \cdot 10^7 \text{ cm/s}$. The theoretical analyses of our
optical data point toward signatures of the ultraviolet
renormalization expected for an interacting Dirac liquid
manifesting in the super-linear temperature dependence
of the Drude weight.

ACKNOWLEDGMENTS

This work was supported by DOE under grant No.
ER 46741-SC0005436 (G.S.J. and H.D.D.) and LPS-
MPO-CMTC (J.H. and S.D.S) and by NSF grant No.
DMR-1104343 (A.B.S.). It was also supported in part
by PRESTO from the Japan Science and Technology
Agency, by Grants-in-Aid for Scientific Research (No.
25707030) and Program for Advancing Strategic Interna-
tional Networks to Accelerate the Circulation of Talented
Researchers (No. R2604) from the Japanese Society for
the Promotion of Science. Some part of the work was per-
formed at the Aspen Center for Physics, partially funded
by NSF Grant No. 1066293. We acknowledge useful con-
versations with A. Vishwanath, Y.B. Kim, P. Goswami,
B. Roy, D. Maslov, N. Perkins and B.I. Shklovskii.

-
- ¹ Dmytro Pesin and Leon Balents, “Mott physics and band
topology in materials with strong spin-orbit interaction,”
Nat Phys **6**, 376 (2010).
- ² Xiao-Liang Qi and Shou-Cheng Zhang, “Topo-
logical insulators and superconductors,”
Reviews of Modern Physics **83**, 1057–1110 (2011).
- ³ M. Z. Hasan and C. L. Kane, “*Colloquium* : Topological
insulators,” Rev. Mod. Phys. **82**, 3045 (2010).
- ⁴ M. Zahid Hasan and Joel E. Moore,
“Three-dimensional topological insulators,”
Annual Review of Condensed Matter Physics **2**, 55–78 (2011).
- ⁵ Su-Yang Xu, Chang Liu, S. K. Kushwaha, T.-R. Chang,
J. W. Krizan, R. Sankar, C. M. Polley, J. Adell, T. Bal-
asubramanian, K. Miyamoto, N. Alidoust, Guang Bian,
M. Neupane, I. Belopolski, H.-T. Jeng, C.-Y. Huang, W.-F.
Tsai, H. Lin, F. C. Chou, T. Okuda, A. Bansil, R. J. Cava,
and M. Z. Hasan, “Observation of a bulk 3d dirac multi-
plet, lifshitz transition, and nested spin states in na3bi,”
arXiv:1312.7624 (2013).
- ⁶ Z. K. Liu, B. Zhou, Y. Zhang, Z. J. Wang, H. M. Weng,
D. Prabhakaran, S.-K. Mo, Z. X. Shen, Z. Fang, X. Dai,
Z. Hussain, and Y. L. Chen, “Discovery of a three-
dimensional topological dirac semimetal, na3bi,” Science
343, 864 (2014).
- ⁷ Madhab Neupane, Su-Yang Xu, Raman Sankar, Nasser
Alidoust, Guang Bian, Chang Liu, Ilya Belopolski, Tay-
Rong Chang, Horng-Tay Jeng, Hsin Lin, Arun Bansil,
Fangcheng Chou, and M. Zahid Hasan, “Observation of
a three-dimensional topological dirac semimetal phase in
high-mobility cd3as2,” Nat Commun **5**, 3786 (2014).
- ⁸ Z. K. Liu, J. Jiang, B. Zhou, Z. J. Wang, Y. Zhang, H. M.
Weng, D. Prabhakaran, S.-K. Mo, H. Peng, P. Dudin,
and et al., “A stable three-dimensional topological dirac
semimetal cd3as2,” Nature Materials **13**, 677–681 (2014).
- ⁹ Sergey Borisenko, Quinn Gibson, Danil Evtushinsky,
Volodymyr Zabolotnyy, Bernd Büchner, and Robert J.
Cava, “Experimental realization of a three-dimensional
dirac semimetal,” Phys. Rev. Lett. **113**, 027603 (2014).
- ¹⁰ Su-Yang Xu, Chang Liu, I. Belopolski, S. K. Kush-
waha, R. Sankar, J. W. Krizan, T.-R. Chang,
C. M. Polley, J. Adell, T. Balasubramanian, and
et al., “Lifshitz transition and van hove singularity
in a three-dimensional topological dirac semimetal,”
Physical Review B **92**, 075115 (2015).
- ¹¹ B. Q. Lv, N. Xu, H. M. Weng, J. Z. Ma, P. Richard,
X. C. Huang, L. X. Zhao, G. F. Chen, C. E. Matt,
F. Bisti, and et al., “Observation of weyl nodes in taas,”
Nature Physics **11**, 724–727 (2015).
- ¹² Su-Yang Xu, Ilya Belopolski, Nasser Alidoust, Madhab
Neupane, Guang Bian, Chenglong Zhang, Raman Sankar,
Guoqing Chang, Zhujun Yuan, Chi-Cheng Lee, and et al.,
“Discovery of a weyl fermion semimetal and topological
fermi arcs,” Science **349**, 613–617 (2015).
- ¹³ Su-Yang Xu, Nasser Alidoust, Ilya Belopolski, Zhu-
jun Yuan, Guang Bian, Tay-Rong Chang, Hao
Zheng, Vladimir N. Strocov, Daniel S. Sanchez,
Guoqing Chang, and et al., “Discovery of a weyl
fermion state with fermi arcs in niobium arsenide,”
Nature Physics **11**, 748–754 (2015).
- ¹⁴ Xiangang Wan, Ari M. Turner, Ashvin Vishwanath, and
Sergey Y. Savrasov, “Topological semimetal and fermi-arc

- surface states in the electronic structure of pyrochlore iridates,” *Physical Review B* **83**, 205101 (2011).
- 15 William Witczak-Krempa, Gang Chen, Yong Baek Kim, and Leon Balents, “Correlated quantum phenomena in the strong spin-orbit regime,” *Annual Review of Condensed Matter Physics* **5**, 57–82 (2014).
 - 16 William Witczak-Krempa, Ara Go, and Yong Kim, “Pyrochlore electrons under pressure, heat, and field: Shedding light on the iridates,” *Physical Review B* **87**, 155101 (2013).
 - 17 Fumiyuki Ishii, Yo Pierre Mizuta, Takehiro Kato, Taisuke Ozaki, Hongming Weng, and Shigeki Onoda, “First-principles study on cubic pyrochlore iridates $y_2\text{ir}_2\text{o}_7$ and $\text{pr}_2\text{ir}_2\text{o}_7$,” *Journal of the Physical Society of Japan* **84**, 073703 (2015).
 - 18 Hiroshi Shinaoka, Shintaro Hoshino, Matthias Troyer, and Philipp Werner, “Phase diagram of pyrochlore iridates: All-in/all-out magnetic ordering and non-fermi-liquid properties,” *Physical Review Letters* **115**, 156401 (2015).
 - 19 Hongbin Zhang, Kristjan Haule, and David Vanderbilt, “Metal-insulator transition and topological properties of pyrochlore iridates,” arXiv:1505.01203 (2015).
 - 20 Kazuyuki Matsuhira, Makoto Wakeshima, Yukio Hinatsu, and Seishi Takagi, “Metal-insulator transitions in pyrochlore oxides $\text{In}_2\text{ir}_2\text{o}_7$,” *Journal of the Physical Society of Japan* **80**, 094701 (2011).
 - 21 S. Nakatsuji, Y. Machida, Y. Maeno, T. Tayama, T. Sakakibara, J. van Duijn, L. Balicas, J. N. Millican, R. T. Macaluso, and Julia Y. Chan, “Metallic spin-liquid behavior of the geometrically frustrated kondo lattice $\text{pr}_2\text{ir}_2\text{o}_7$,” *Physical Review Letters* **96**, 087204 (2006).
 - 22 Yo Machida, Satoru Nakatsuji, Shigeki Onoda, Takashi Tayama, and Toshiro Sakakibara, “Time-reversal symmetry breaking and spontaneous hall effect without magnetic dipole order,” *Nature* **463**, 210–213 (2010).
 - 23 Hiroshi Takatsu, Kunihiko Watanabe, Kazuki Goto, and Hiroaki Kadowaki, “Comparative study of low-temperature x-ray diffraction experiments on $\text{r}_2\text{ir}_2\text{o}_7$ ($\text{r}=\text{nd}$, eu , and pr),” *Physical Review B* **90**, 235110 (2014).
 - 24 K. Ueda, J. Fujioka, Y. Takahashi, T. Suzuki, S. Ishiwata, Y. Taguchi, and Y. Tokura, “Variation of charge dynamics in the course of metal-insulator transition for pyrochlore-type $\text{nd}_2\text{ir}_2\text{o}_7$,” *Physical Review Letters* **109**, 136402 (2012).
 - 25 Y. Lee, S. Moon, Scott Riggs, M. Shapiro, I. Fisher, Bradford Fulfer, Julia Chan, A. Kemper, and D. Basov, “Infrared study of the electronic structure of the metallic pyrochlore iridate $\text{bi}_2\text{ir}_2\text{o}_7$,” *Physical Review B* **87**, 195143 (2013).
 - 26 Jun J. Ishikawa, Eoin C. T. O’Farrell, and Satoru Nakatsuji, “Continuous transition between antiferromagnetic insulator and paramagnetic metal in the pyrochlore iridate $\text{eu}_2\text{ir}_2\text{o}_7$,” *Phys. Rev. B* **85**, 245109 (2012).
 - 27 See Supplemental Material at <http://link.aps.org/supplemental/10.1103/PhysRevB.92.241108> for more details on fitting procedures.
 - 28 A. B. Kuzmenko, “Kramers–kronig constrained variational analysis of optical spectra,” *Review of Scientific Instruments* **76**, 083108 (2005).
 - 29 John F. McCaffrey, Neil T. McDevitt, and Conrad M. Phillippi, “Infrared lattice spectra of rare-earth stannate and titanate pyrochlores,” *J. Opt. Soc. Am.* **61**, 209–212 (1971).
 - 30 L. Hozoi, H. Gretarsson, J. P. Clancy, B.-G. Jeon, B. Lee, K. H. Kim, V. Yushankhai, Peter Fulde, D. Casa, T. Gog, and et al., “Longer-range lattice anisotropy strongly competing with spin-orbit interactions in pyrochlore iridates,” *Physical Review B* **89**, 115111 (2014).
 - 31 Robert E. Throckmorton, Johannes Hofmann, Edwin Barnes, and S. Das Sarma, “Many-body effects and ultraviolet renormalization in three-dimensional dirac materials,” *Physical Review B* **92**, 115101 (2015).
 - 32 S. Das Sarma and E. H. Hwang, “Charge transport in gapless electron-hole systems with arbitrary band dispersion,” *Phys. Rev. B* **91**, 195104 (2015).
 - 33 Johannes Hofmann and S. Das Sarma, “Plasmon signature in dirac-weyl liquids,” *Physical Review B* **91**, 241108 (2015).
 - 34 Dmitri E. Kharzeev, Robert D. Pisarski, and Ho-Ung Yee, “Universality of plasmon excitations in dirac semimetals,” arXiv:1412.6106 (2014).
 - 35 M. Orlita, D. M. Basko, M. S. Zholudev, F. Teppe, W. Knap, V. I. Gavrilenko, N. N. Mikhailov, S. A. Dvoret-skii, P. Neugebauer, C. Faugeras, and et al., “Observation of three-dimensional massless kane fermions in a zincblende crystal,” *Nature Physics* **10**, 233–238 (2014).
 - 36 T. Timusk, J. P. Carbotte, C. C. Homes, D. N. Basov, and S. G. Sharapov, “Three-dimensional dirac fermions in quasicrystals as seen via optical conductivity,” *Physical Review B* **87**, 235121 (2013).
 - 37 R. Y. Chen, S. J. Zhang, J. A. Schneeloch, C. Zhang, Q. Li, G. D. Gu, and N. L. Wang, “Optical spectroscopy study of the three-dimensional dirac semimetal zrte_5 ,” *Physical Review B* **92**, 075107 (2015).